Luminescence thermometry and field induced slow magnetic relaxation based on a near infrared emissive heterometallic complex†

Konstantinos Karachousos-Spiliotakopoulos, [ID] [a] Vassilis Tangoulis, [ID] *[a] Nikos Panagiotou, [ID] [b] Anastasios Tasiopoulos, [ID] [b] Eufemio Moreno-Pineda, [ID] [c] Wolfgang Wernsdorfer, [ID] *[d,e] Michael Schulze, [ID] [e] Alexandre M. P. Botas[f] and Luis D. Carlos [ID] *[f]

The 1 : 1 : 1 reaction of $YbCl_3 \cdot 6H_2O$, $K_3[Co(CN)_6]$ and $bpyO_2$ in H_2O has provided access to a complex with formula $[YbCo(CN)_6(bpyO_2)_2(H_2O)_3] \cdot 4H_2O$ (**1**) in a very good yield while its structure has been determined by single-crystal X-ray crystallography and characterised based on elemental analyses and IR spectra. Magnetic susceptibility studies showed the complex to be a field induced single molecule magnet, as confirmed by μ-SQUID measurements. CASSCF calculations confirm the existence of a $m_J = 7/2$ ground state, with rather large transverse components, responsible for the fast relaxation characteristic of compound **1** at zero DC field, which is reduced upon application of DC fields. Moreover, a combination of luminescence studies along with CASSCF calculation allows the identification of the band structure of the complex, which is ultimately related to its electronic properties. Compound 1 operates as a luminescent thermometer in the 125–300 K range with a maximum relative thermal sensitivity of ≈0.1% K^{-1} at 180 K.

Introduction

In the middle of the last decade,[1] an impressive outburst of interest occurred in the scientific community for light-emitting micro and/or nanomaterials acting as remote temperature sensors at nanoscale where classical thermometers failed to operate.[2–6] Since that time, many diverse scientific fields are influenced by luminescence thermometry such as *in vivo* and *in vitro* sensing in biomedicine,[7–13] magnetism,[14–27] catalysis,[28,29] and microelectronics.[30,31]

[a]*Department of Chemistry, Laboratory of Inorganic Chemistry, University of Patras, 26504 Patras, Greece. E-mail: vtango@upatras.gr*

[b]*Department of Chemistry, University of Cyprus, Nicosia 1678, Cyprus*

[c]*Depto. de Química-Física, Escuela de Química, Facultad de Ciencias Naturales, Exactas y Tecnología, Universidad de Panamá, Panamá, Panamá*

[d]*Institute for Quantum Materials and Technology (IQMT), Karlsruhe Institute of Technology (KIT), Hermann-von-Helmholtz-Platz 1, D-76344 Eggenstein-Leopoldshafen, Germany*

[e]*Physikalisches Institut, Karlsruhe Institute of Technology, D-76131 Karlsruhe, Germany*

[f]*Phantom-g, CICECO – Aveiro Institute of Materials, Department of Physics, University of Aveiro, 3810-193 – Aveiro, Portugal*

In the field of molecular magnetism,[32,33] the phenomenon of luminescence in Single Molecule Magnets (SMMs) is of great importance for a detailed investigation of the underlying mechanisms of the magnetisation relaxation in mononuclear, dinuclear and/or heteronuclear lanthanide(III) complexes.[22,27] High resolution temperature dependent photoluminescence studies can, in principle, determine spectroscopically the Stark sublevels of the Ln(III) ions and provide a direct comparison with those derived from magnetic and theoretical *ab initio* studies.[14–27,34–38] A promising and quite exciting research area is covering the phenomenon of SMM luminescence thermometry where the slow magnetic relaxation characteristics of the lanthanide are combined with its luminescence properties to provide the next generation of thermometers able to monitor temperature changes in real-time during the operation of the electronic device.[5,16,22] Replacing conventional contact-type thermometers with luminescent SMM-based devices seems to be the key to understanding: (a) the principles and laws of the heat generation in devices; and (b) the effective monitoring of the temperature during the operation of the device without perturbing the system.[5] An ideal situation for an SMM luminescence thermometer is to provide an overlap of the two properties, magnetic and optical, in the working temperature offering the unique opportunity for monitoring the temperature in a contactless way at low temperatures in which the magnetic behaviour of the SMM molecule as well as spectral

changes are revealed.[16] Having in mind that thermally activated mechanisms of magnetisation relaxation may affect the luminescence properties of an individual SMM molecule in various ranges of temperature, the thermal probing capabilities of the luminescent SMM-based device can be expanded at higher temperatures. Another exciting feature of these devices is the optomagnetic sensitivity due to the conservation of the luminescent thermometer properties under the application of external magnetic fields.[15,16]

It has been well documented that the derivatives of heterocyclic ligands bearing *N*-oxide functions sensitise efficiently the emission of Ln(III) ions upon UV radiation.[39,40] More explicitly, it was found that there is a profound influence of the 2,2′-bipyridine-*N*,*N*′-dioxide ($bpyO_2$)[40–42] ligand, replacing the two aqua ligand molecules, in the inner sphere of a Eu(III) complex $[Eu(hfac)_3(H_2O)_2]$ where hfac = hexafluoroacetylacetonate(−1) ligand. A 15-fold increase of the quantum yield has been reported for the complex $[Eu(hfac)_3(bpyO)_2]$ indicating that the ancillary $bpyO_2$ ligand provided excellent sensitisation being solely responsible for the $\frac{3}{4}$ of the total energy transfer.

Inspired by previous works, we decided to investigate the phenomenon of SMM luminescent thermometry using the blending of CN⁻/$bpyO_2$ ligands on heterometallic 3d/4f-metal complexes. In order to succeed in this, we used the red-emissive octahedral diamagnetic $[(CoCN)_6]^3$ linker as an alternative source for effective energy transfer to 4f-metal ions. Following this strategy we have recently reported a new multifunctional hetero-dinuclear compound $[DyCo^{III}(CN)_6(bpyO_2)_2(H_2O)_3]\cdot 4H_2O$,[43] exhibiting both SMM magnetic properties and temperature-dependent photoluminescent characteristics. High resolution optical studies revealed a maximum thermal sensitivity of 1.84% K⁻¹ at 70 K, which is higher than the acceptable sensitivity boundary of 1% K⁻¹ for high performance luminescence thermometers in a broad range of temperatures between 40–140 K. Magnetic studies showed slow relaxation upon application of a DC field. Replacing the Co^{III} metal ion with the Fe^{III} ion, we managed to isolate the isomorphous antiferromagnetic coupled Dy–Fe pair, $[DyFe^{III}(CN)_6(bpyO_2)_2 (H_2O)_3]\cdot 4H_2O$[43] featuring SMM properties but unfortunately its emission is governed by the $bpyO_2$ ligand due to the quenching of the external carriers in the Fe^{III} ion. Finally, two isomorphous and structurally characterised heterodimers have been reported, of the type $[LnFe^{III}(CN)_6(bpyO_2)_2(H_2O)_3]$ where (Ln = Sm, Gd).[44,45] The abovementioned heterodimers enrich the small family of homometallic[40,42,46] or heterometallic[41,44,45] complexes where the Ln^{III} centre is coordinated to $bpyO_2$ molecules. Recently, Chorazy *et al.*[27] reported the magnetic and luminescent characterisation of emissive $[Yb^{III}(bpyO_2)_4]^{3+}$ SMMs by the crystallisation with (thio)-cyanidometallate counterions. The SMM behaviour in the whole family is mainly dominated by the Raman relaxation and is dependent on the (thio)cyanido counterion. Quite interestingly, the *ab initio* theoretical study confirmed the optically estimated value of the energy gap ($\Delta E >$ 120 cm⁻¹) of the two lowest-lying Kramers doublets indicating the lack of an Orbach relaxation.

Anticipating that the blending of the $[Co(CN)_6]^3$ linker with the $bpyO_2$ ligand would efficiently sensitise the NIR emissive Yb(III) ion, we pursued our research efforts for the synthesis and physicochemical study of the Yb(III)/Co(III) hetero-dinuclear compound as a potential SMM Luminescent thermometer.

Experimental

Materials, physical techniques and spectroscopic methods

All manipulations were performed under aerobic conditions. $YbCl_3\cdot 6H_2O$, $K_3[Co(CN)_6]$ and $bpyO_2$ were purchased from commercial sources. Elemental analyses were performed by the University of Patras microanalytical service. FT-IR spectra (4000–450 cm⁻¹) were recorded using a PerkinElmer 16PC spectrometer with samples prepared as KBr pellets.

Magnetic measurements

The magnetic susceptibility data for 1 was collected using a Quantum Design MPMS®3 and MPMS-XL SQUID magnetometers on polycrystalline samples in the range of 2–300 K with applied fields (H) ranging from 0 to 5 kOe. AC data was collected using an oscillating magnetic field of 3.5 Oe and frequencies between 1 and 1.5 kHz. DC data were corrected for diamagnetic contributions from the eicosane and core diamagnetism employing Pascal's constants.[4] Low temperature (0.03–2 K) magnetisation measurements were performed on single crystals using a μ-SQUID apparatus at different sweep rates between 0.002 and 0.280 T s⁻¹. The time resolution is approximately 1 ms. The magnetic field can be applied in any direction of the μ-SQUID plane by separately driving three orthogonal coils. The magnetic field was applied parallel to the easy axis of magnetisation employing the transverse field method.

Luminescence measurements

The photoluminescence spectra in the NIR spectral range were recorded with a modular double grating excitation spectrofluorimeter with a TRIAX 320 emission monochromator (Fluorolog-3, Horiba Scientific) coupled to a H9170 Hamamatsu photomultiplier, using a front face acquisition mode. The excitation source was a 450 W Xe arc lamp. The temperature was varied using a helium-closed cycle cryostat, a vacuum system (4 × 10⁻⁴ Pa), and an autotuning temperature controller (Lakeshore 330, Lakeshore) with a resistance heater. All the measurements began at least 300 s after the temperature indicated in the temperature controller remained constant, thus ensuring the thermalization of the samples and constant temperature during the measurement.

Preparation of $[YbCo(CN)_6(bpyO_2)_2(H_2O)_3]\cdot 4H_2O$ (1)

The organic ligand $bpyO_2$ (15.0 mg, 0.07 mmol) was dissolved in 0.6 mL of warm distilled H_2O and a pale yellow solution was obtained. Subsequently, solid $YbCl_3\cdot 6H_2O$ (27.0 mg, 0.07 mmol) was added to the former solution to obtain solu-

tion 1. Furthermore, $K_3[Co(CN)_6]$ (23.0 mg, 0.07 mmol) was dissolved in 0.6 mL distilled H_2O in order to obtain solution 2. Then, solution 2 was added to solution 1 under mild stirring. The resulting pale-yellow solution was stored in a closed vial at room temperature. In a period of 24 h X-ray quality, white needle shaped crystal appeared. The final product was collected via filtration. Typical yields were in the range of 45–55% (based on the bpyO$_2$ available). The same complex is obtained from the stoichiometrically "correct" Yb^{III} : Co^{III} : bpyO$_2$ 1 : 1 : 2 reaction ratio (IR and microanalytical evidence).

Analytical data calculated for $C_{26}H_{16}CoN_{10}O_{11}$ Yb (found values are in parentheses): C 35.63 (35.27), H 1.84 (1.99), N 15.98 (15.81) %. IR bands (KBr, cm^{-1}): 3380s, 3126s, 3097w, 3083w, 2165w, 2123s, 1654m, 1475s, 1446m, 1427s, 1319w, 1295w, 1259s, 1245s, 1220s, 1160w, 1124w, 1106w, 1052w, 1033m, 881w, 858m, 838m, 782s, 773s, 732w, 717w, 636w, 593m, 578m, 561w, 536m, 518m, 487w, 449w, 422w.

For the magnetic and optical studies, single crystals of the product were used which were carefully powdered prior to measurements.

Single crystal X-ray crystallography

Single crystal X-ray diffraction data were collected on an Oxford-Diffraction Supernova diffractometer, equipped with a CCD area detector utilizing Mo-Kα (λ = 0.71073 Å) radiation. Suitable crystals were attached to glass fibres using paratone-N oil and transferred to a goniostat where they were cooled for data collection. Empirical absorption corrections (multi-scan based on symmetry-related measurements) were applied using CrysAlis RED software.[47] The structures were solved by direct methods with SHELXT[48] and refined on F^2 using full-matrix least squares with SHELXL-2014/7.[48] Software packages used: CrysAlis CCD for data collection,[47] CrysAlis RED for cell refinement and data reduction,[47] and WINGX for geometric calculations.[49] The non-H atoms were treated anisotropically, whereas the H atoms were placed in calculated, ideal positions and refined as riding on their respective carbon atoms. Unit cell parameters and structure solution and refinement data for Yb/Co are listed in Table S1.†

Results and discussion

Crystal structure

The crystal structure of $[YbCo(CN)_6(bpyO_2)_2(H_2O)_3]·4H_2O$ (1), was determined by single-crystal X-ray crystallography and the structural plot of compound 1 is shown in Fig. 1 while crystallographic data are shown in Tables S1 and S2.† The complex crystallises in the triclinic $P\bar{1}$ space group while a molar ratio 1 : 4 exists between the heterodinuclear $[YbCo(CN)_6(bpyO_2)_2(H_2O)_3]$ molecule and the lattice solvent H_2O molecules. The bridging between the Ln(III) and Co(III) centres in the dinuclear molecule is succeeded by a cyano group (Ln–N≡C–M). The 8-coordination at Ln^{III} is completed by two O, O′-bidentate chelating bpyO$_2$ molecules and three aqua ligands, while there are five terminal C-bonded cyano groups
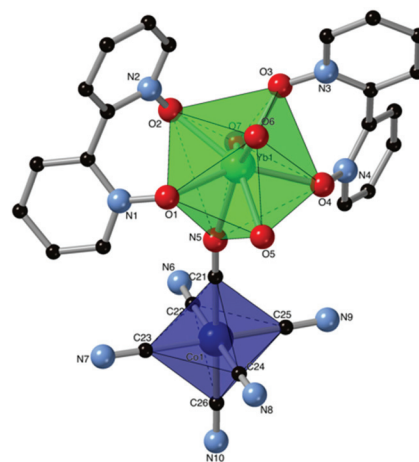

Fig. 1 Partially labelled plot of the structure of the molecule [YbCo(CN)$_6$(bpyO$_2$)$_2$(H$_2$O)$_3$] in the crystal of compound 1·4H$_2$O.

in the coordination sphere of the transition metal ion leading to coordination spheres of {Ln^{III}O$_7$N} and {Co^{III}C$_6$}. The bond lengths Co^{III}–C [1.881(5)–1.907(5) Å] indicate that the Co^{III} is a low-spin 6-coordinate metal ion.[50,51] The Yb^{III}–O/N bond distances [2.246(3)–2.424(4) Å] for compound 1 are in the typical ranges for lanthanide complexes containing 8-coordinate Yb^{III} ions.[14,17,24,27,35] Concerning the bond lengths between carbon and nitrogen of the cyano groups, the range is 1.132(6)–1.157(6). A skew 7-membered chelating ring is formed between the bpyO$_2$ ligand and the Yb^{III} centre. There is a slight lengthening of the nitrogen–oxygen of the pyridine-N-oxide moieties of the bpyO$_2$ ligand from 1.302(2) Å (which corresponds to the free bpyO$_2$ ligand)[52] to 1.328(5)–1.341(4) Å denoting the coordination of the ligand to the lanthanide ion.

In the IR spectra of compound 1 there are two strong bands at ~3300 and ~3100 cm^{-1} due to the ν(OH) vibration of the lattice and coordinated H$_2$O molecules, respectively[53] while the δ(OH) vibration of H$_2$O appears at ~1650 cm^{-1}. The broadness of the bands suggests the existence of H-bonding interactions between the H$_2$O molecules. The stretching vibrations of the heterocyclic rings of coordinated bpyO$_2$[42] appear in the 1560–1420 cm^{-1} region slightly shifted compared to those of free bpyO$_2$. The band at 1218 cm^{-1} is assigned[42] to the ν(N–O) vibration (shifted from the value of 1260 cm^{-1} observed for the free ligand) indicating the O,O′-coordination of the ligand. The strong band at 2124 cm^{-1} in the spectra of 1 is assigned[54] to the ν(C≡N) mode of the terminal C-bonded cyano ligands. Two ν(C≡N) bands are expected since one of the cyano groups is in bridging mode. The band for the bridging cyano group is situated at a higher wavenumber than for the terminal cyanido groups.[54] In our case, this band is observed in the spectra at 2157 cm^{-1} and it is assigned to the ν(C≡N) mode of the bridging cyanido group (Fig. S1†).

The coordination geometry of the Co(III) ion in the heterodinuclear complex is octahedral, where the trans C–Co^{III}–C angles are in the range 177.0(4)–179.0(2)° and the bond angle

Co–C≡N [177.0(4)–178.7(5)] presents minor deviation from linearity. In order to investigate the coordination polyhedron around the Yb^{III} centre, the SHAPE[55] software was used, and it was found that the triangular dodecahedron is the ideal polyhedron (Table S3†). The calculated Yb–N≡C angle of ~165.9°, denotes a significant bending of the intermetallic cyano bridge which is direct evidence of the steric hindrance on Yb^{III} created from the two $bpyO_2$ ligands. The heterodinuclear molecules are inter-connected through a rich hydrogen network between the lattice H_2O molecules and the five terminal cyano groups of the $\{Co^{III}(CN)_6\}^{3-}$ moieties creating a 3D robust architecture consisted of 2D pseudo layers parallel to the *ab* plane (Fig. S2a†) which are further connected through hydrogen bonding and π⋯π stacking interactions with adjacent layers in the *c* direction (Fig. S2b†). The water lattice molecules are filling the interlayer space and participate in H bonds with their O atoms (both donors and acceptors) while the coordinated H_2O molecule form two H bonds with the donor O atom.

Magnetic measurements

The investigation of the magnetic characteristics of compound **1** was carried out in a SQUID magnetometer employing a polycrystalline powdered sample. Fig. S3† shows the $\chi_M T(T)$ static magnetic susceptibility for compound **1** in an applied magnetic field of 1 kOe (χ_M is the molar magnetic susceptibility) and the molar magnetisation as function of field ($M(H)$). As

can be observed, the room temperature value of $\chi_M T$ for compound **1** is 2.65 cm^3 mol^{-1} K very close to the expected for an isolated Yb(III) ion, *i.e.* 2.57 cm^3 mol^{-1} K ($^2F_{7/2}$, $J = 7/2$, $g = 8/7$). Upon decreasing temperatures, the $\chi_M T(T)$ profile decreases continuously reaching a minimum value of 1.93 cm^3 mol^{-1} K at the lowest temperature (2 K). The decrease observed in the $\chi_M T(T)$ data can be attributed to the depopulation of crystal field levels. Furthermore, the saturation value of M, at 7 T, is 2.15μ_B implying an $m_J = \pm 7/2$ ground state.

In order to determine whether compound **1** possess slow relaxation dynamics, alternating current (AC) magnetic susceptibility studies were carried out employing an oscillating field of 3.5 Oe. No SMM behaviour was observed at zero DC field, indicating fast relaxation in the complex; however, a clear SMM behaviour was identified upon application of a DC field. Fig. 2a and b show the temperature $\chi''_M(T)$ and the frequency dependent out-of-phase magnetic susceptibility $\chi''_M(\nu)$ upon application of 1.25 kOe DC field, respectively while in Fig. S4 and S5† is shown the temperature $\chi'_M(T)$ and the frequency dependent magnetic susceptibility $\chi'_M(\nu)$ upon application of the same DC field. In the $\chi''_M(T)$ a frequency dependent maximum at *ca.* 5.5 K (1512 Hz) is observed, while in the $\chi''_M(\nu)$ a maximum is defined ranging between 2.0 and 5.2 K. Upon increasing temperatures, the $\chi''_M(\nu)$ maximum shifts towards higher frequencies, indicating the temperature dependent regime. Extraction of $\tau(T)$ by fitting the Cole–Cole plot to a single process, in the temperature range where the
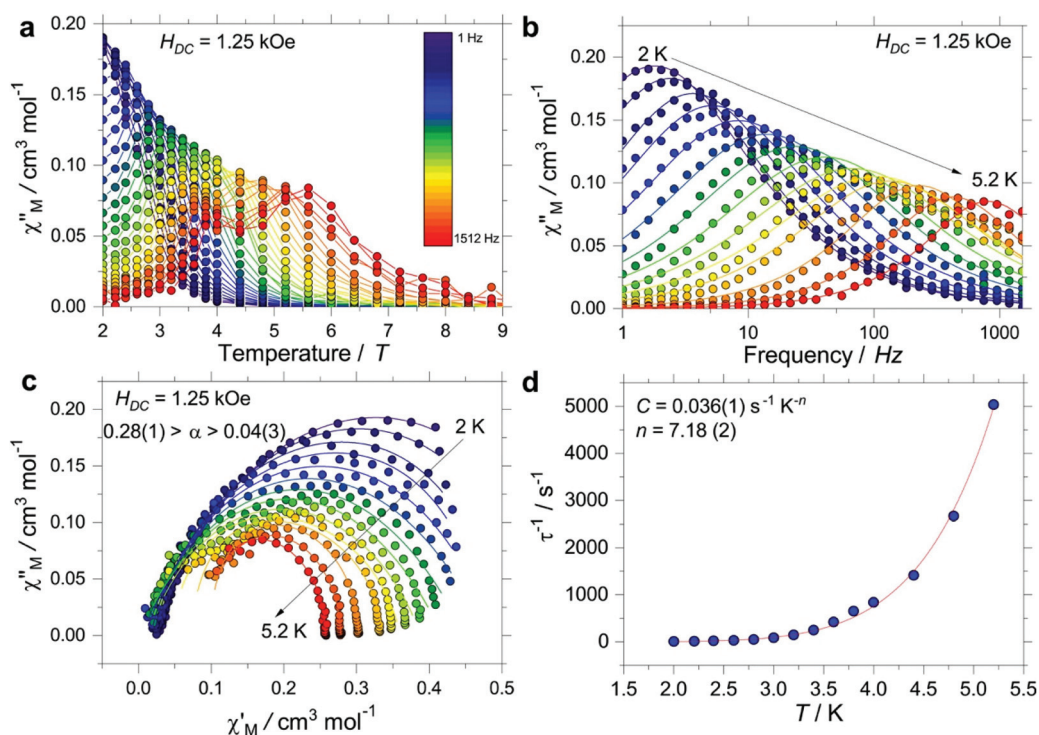
Fig. 2 (a) Experimental $\chi''_M(T)$ H_{DC} = 1.25 kOe; (b) $\chi''_M(\nu)$ with H_{DC} = 1.25 kOe. (c) Cole plots ($\chi''_M(\nu)$ *vs.* $\chi'_M(\nu)$) showing a single relaxation process (d) τ *vs.* 1/T plots of AC data at zero field and Arrhenius treatment for AC data. Solid lines in panel (b) and (c) are the fit to a single Debye process for compound **1**, while in (d) the solid line represent the $\tau(T)$ considering the Raman process: $\tau^{-1} = CT^n$.
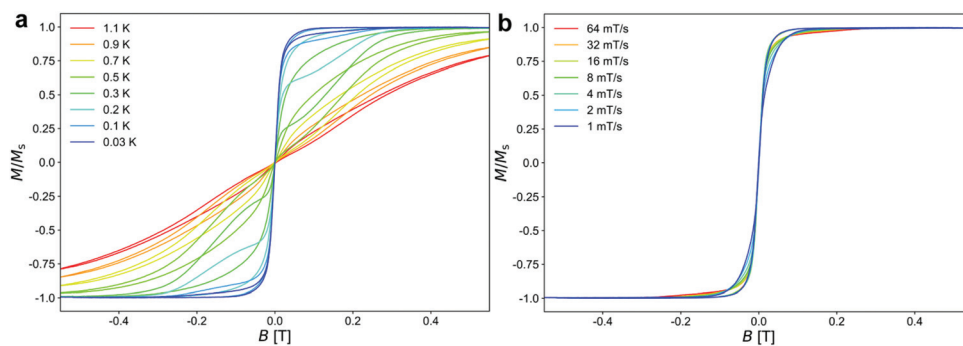
Fig. 3 (a) μ-SQUID loops obtained from single crystals measurements of compound **1** at a fix field-sweep rate of 64 mT s^{-1} and (b) the temperature dependence at a based temperature of 30 mK.

maximum occurs, and fitting the $\tau(T)$ considering the Raman and Orbach processes employing eqn (1):

$$\tau^{-1} = CT^n \qquad (1)$$

leads to the following parameters: $C = 0.0036(1)$ s^{-1} K^{-n}, $n = 7.18(2)$ and $0.28(1) > \alpha > 0.04(3)$ indicating a relatively wide distribution of processes and fast relaxation (Fig. 2d). Although the n value is smaller than the expected $n = 9$ for Kramers ions, values of n as low as 2 have reported for Yb(III) field induced SIMs.[56] Note that the relaxation dynamics is characterised by the Raman processes, thus, inducing fast relaxation, as observed at zero field. Application of a DC field, brings the systems out of the fast relaxation regime, thus, revealing the SMM character of compound **1**.

To confirm the observed slow relaxation characteristics of compound **1**, μ-SQUID studies were performed down to 30 mK and with field sweep rates ranging from 1 to 64 mT s^{-1}. For this, single crystals of compound **1** were measured in a μ-SQUID array with the field aligned along the easy axis of the crystal. The field was applied along the easy axis of the crystal employing a 3D vector magnet and the transverse field method. The so-collected loops revealed a waist-constricted typical loops commonly observed in single-ion lanthanide-based SMMs (Fig. 3). The loops are temperature and sweep-field dependent and exhibit a small opening at the lowest temperature and fastest scan rates, with a sharp transition at zero field, characteristics of strong Quantum Tunnelling of the Magnetisation (QTM). The observed behaviour is consistent with the AC susceptibility studies, where no SMM behaviour was observed at zero DC field, whilst upon application of a DC field revealed the SMM character in compound **1**.

Ab initio calculations

Further insight into the magnetic characteristic of compound **1** was gained *via ab initio* calculations employing the CASSCF/SO-RASSI/SINGLE_ANISO approach implemented in the OpenMolcas package.[57–59] The crystal structure of compound **1** was employed without further optimisations with the atoms being described by the standard basis sets from the ANO-RCC library.[57–59] A basis set of VTZP quality was employed for the

Yb(III) ion, whilst VDZP quality was used for atoms directly bound to the Yb(III) ions, and VDZ quality for the remaining atoms. The molecular orbitals (MOs) were optimised in state-averaged CASSCF calculations. The active space was defined by the thirteen 4f electrons in the seven 4f orbitals of Yb(III). With 7 roots were included for $S = 1/2$, (RASSCF routine). The wavefunctions obtained from these CASSCF calculations were posteriorly mixed by spin–orbit coupling, employing the RASSI routine. Finally, the crystal field decomposition of the ground $J = 7/2$ multiplet of the $^2F_{7/2}$ term was executed with the SINGLE_ANISO module.[57] The simulations obtained employing the CASSCF results are shown as solid lines in Fig. S3.†

A ground doublet state with g values $g_x = 0.1627$, $g_y = 0.1868$, and $g_z = 7.6755$, was found, indicating some axiality in compound **1**, with considerable rhombic anisotropy. The first excited state is found to lie at 347 cm^{-1} with the second excited state at 443 cm^{-1} and the third excited state at 514 cm^{-1}. The main magnetic axis (z) on the Yb(III) ion is indicated in Fig. 4 by the orange arrow. It is important to highlight that the magnitude of the energy barrier obtained for compound **1** is lower than the separation between the first excited
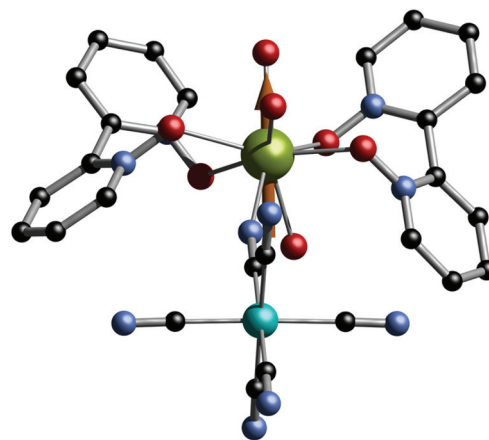
Fig. 4 Direction of the principal axis of the g-tensor in the ground Kramer doublet of compound **1**. Colour code: Co, cyan; Yb, green; O, red; C, black; N, pale blue. Hydrogens omitted for clarity.

state and the ground state obtained from CASSCF calculation, which indicates an under-barrier process.[60] Considering the average matrix elements of magnetic moment between the electronic states, it can be seen that relaxation is readily possible at the ground and through excited states, hence, the fast relaxing characteristics of compound **1**.

It should be noted here that it was not possible to simulate the significant decrease of the experimental $\chi_M T$ for temperatures lower than 30 K. Similarly, there are visible differences between the experimental and calculated $M(H)$. These differences could be a consequence of depopulation of the crystal field levels and solvent and/or packing effects, not taken into account by CASSCF due to the limitations of these calculations which are performed in the gas phase, *i.e.* considering a perfectly isolated molecule, without neighbouring molecules. Experimentally, however, neighbouring complexes, as well as solvent molecules might induce some distortion and effects not considered in the calculation, hence producing some small differences between the experimentally obtained data and the theoretical traces.

The possibility of dipolar intermolecular antiferromagnetic interactions has been ruled out since the closest Yb(III)···Yb(III) contact in the crystal packing of compound **1** is of 7.983 Å,

which might indicate very small intermolecular interactions at such high temperatures (<0.01 cm^{-1}, from a point dipolar analysis). In this regards, μ-SQUID is more suitable for the detection of such small interaction. However, as observed in Fig. 3, the μ-SQUID loops do not exhibit the typical waist restricted loops characteristic of antiferromagnetically coupled systems. Hence, we conclude that any intermolecular interaction is too small to be sizable in μ-SQUID (in temperatures as low as 30 mK) and therefore would be unnoticeable in the experimental $\chi_M T$ data (with temperatures above 2 K).

Luminescence measurements

The room-temperature emission spectra of compound **1**, under 315 nm excitation, reveals the characteristic luminescence of Yb^{3+} in the near-infrared range ascribed to the $^2F_{5/2} \rightarrow {}^2F_{7/2}$ transition (Fig. 5a). Due to the crystal field splitting of the $^2F_{5/2}$ and $^2F_{7/2}$ levels, the emission spectra (16–300 K) are deconvoluted into 8 Kramers doublets, as exemplified in Fig. 5b for the spectrum recorded at 16 K. The transitions were identified considering the results of the theoretical studies mentioned above and the corresponding energy level scheme is shown in Fig. 5c where the higher energy line involves the first excited Kramers doublet of the $^2F_{5/2}$ multiplet (R$_2$) and
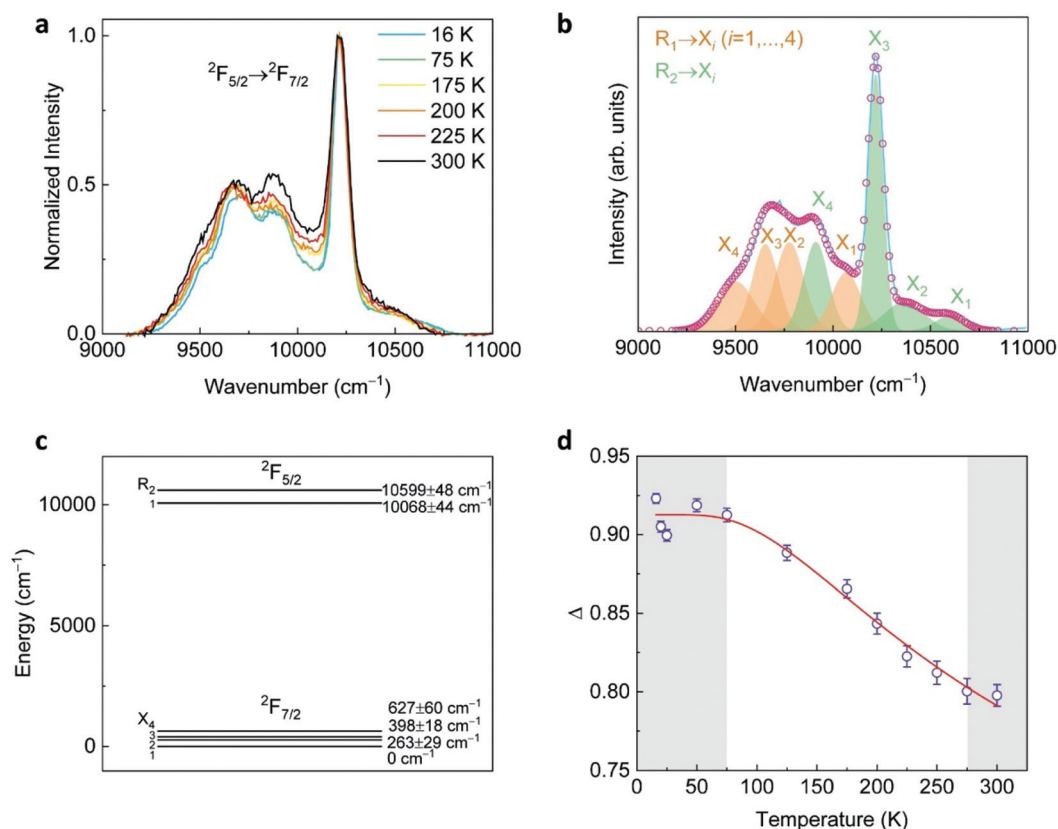
Fig. 5 (a) Emission spectra of compound **1** in the region of the $^2F_{5/2} \rightarrow {}^2F_{7/2}$ transition under 315 nm excitation for selected temperatures. (b) Emission spectrum (acquired at 16 K) with a multi-Gaussian functions envelope fit [r^2 > 0.99] (open circles) and the components (orange/green shadowed Gaussians) arising from the ground (R$_1$) and first (R$_2$) $^2F_{5/2}$ Kramers doublets to the $^2F_{7/2}$ multiplet (X$_{1-4}$). (c) Simplified energy level diagram. (d) Temperature dependence of the thermometric parameter. The line represents the best fit [r^2 > 0.96] to the data using eqn (2). The shadowed areas mark the regions in which the thermometer is out of the operating range.

the $^2F_{7/2}$ ground level (X_1). A reasonable agreement between the predicted and measured energies is obtained.

Since *a priori* there is no reason to select a particular pair of $^2F_{5/2} \rightarrow {}^2F_{7/2}$ lines to define the thermometric parameter Δ, we consider $\Delta = I_2/I_1$, where I_2 and I_1 are the integrated intensities of the four transitions originated from R_2 and R_1, respectively (Fig. 5c). Fig. 5d shows the temperature dependence of the thermometric parameter, which can be well described by the classical Mott-Seitz model involving one deactivation channel:[61]

$$\Delta = \frac{I_2}{I_1} = \frac{\Delta_0}{1 + \alpha e^{\frac{\Delta E}{k_B T}}}, \qquad (2)$$

where k_B is the Boltzmann constant, T the absolute temperature, Δ_0 the thermometric parameter at $T = 0$ K, α the ratio between the nonradiative and radiative transition probabilities, and ΔE the activation energy for the thermal quenching process. Fitting the temperature dependence of the experimental Δ values to eqn (2) yields $\Delta_0 = 0.91 \pm 0.01$, $B = 0.6 \pm 0.2$, and $\Delta E = 267 \pm 53$ cm^{-1}.

Below 125 K and above 275 K, the Δ values change within the error meaning that for these temperature ranges the thermometer is out of the so-called operating range. The performance of the thermometer was evaluated using the relative thermal sensitivity (S_r) and the temperature uncertainty (δT) (Fig. S6†). The temperature dependence of S_r presents a maximum value of $\approx 0.1\%$ K^{-1} at 180 K, the corresponding minimum δT is ≈ 4 K, Fig. S5.† Such a low S_r value is expected as the thermometric parameter considers the intensities of two Kramers doublets.[24,62] Moreover, although there are two examples of Yb^{3+}-based complexes operating as SMMs and thermometric probes with S_r values $\approx 1\%$ K^{-1}, a value of the same order of magnitude of that presented here ($\approx 0.15\%$ K^{-1} at 300 K) was reported in the third known example.[17]

Conclusions

We reported a new multifunctional hetero-dinuclear compound $[YbCo^{III}(CN)_6(bpyO_2)_2(H_2O)_3] \cdot 4H_2O$ (**1**), featuring SMM magnetic properties and temperature-dependent photoluminescent characteristics. AC studies show compound **1** to be a field induced SMM upon application of a DC field, while μ-SQUID measurements reveal field and temperature dependent loops, characteristics of SMMs. The reasoning for the fast relaxation dynamics at zero field was rationalised by CASSCF calculations, indicating that transverse components are rather important for promoting relaxation. Luminescence studies agree with CASSCF calculations, while the SMM character and luminescent characteristic of compound **1** makes it an interesting system for optospintronic applications.[63,64] This work introduces a new example to the scarcely explored field of SMM luminescence thermometry despite its relatively low thermographic performance. The optimization of the thermometric features is usually achieved through a serendipity approach, but it still appears difficult to accurately predict the

sensing performance. The smart engineering of SMM luminescent devices requires the establishment of comprehensive guidelines able to explain and predict their thermometric behaviour.[65,66]

Conflicts of interest

There are no conflicts to declare.

Acknowledgements

References

1 S. W. Allison, *Meas. Sci. Technol.*, 2019, **30**, 072001.
2 C. D. S. Brites, P. P. Lima, N. J. O. Silva, A. Millan, V. S. Amaral, F. Palacio and L. D. Carlos, *Nanoscale*, 2012, **4**, 4799–4829.
3 M. D. Dramicanin, *J. Appl. Phys.*, 2020, **128**, 040902.
4 D. Jaque and F. Vetrone, *Nanoscale*, 2012, **4**, 4301–4326.
5 M. Quintanilla and L. M. Liz-Marzan, *Nano Today*, 2018, **19**, 126–145.
6 H. Suo, X. Q. Zhao, Z. Y. Zhang, Y. Wang, J. S. Sun, M. K. Jin and C. F. Guo, *Laser Photonics Rev.*, 2021, **15**, 2000319.
7 A. Bednarkiewicz, L. Marciniak, L. D. Carlos and D. Jaque, *Nanoscale*, 2020, **12**, 14405–14421.
8 E. Hemmer, P. Acosta-Mora, J. Mendez-Ramos and S. Fischer, *J. Mater. Chem. B*, 2017, **5**, 4365–4392.
9 N. Inada, N. Fukuda, T. Hayashi and S. Uchiyama, *Nat. Protoc.*, 2019, **14**, 1293–1321.
10 R. Pinol, J. Zeler, C. D. S. Brites, Y. Y. Gu, P. Tellez, A. N. C. Neto, T. E. da Silva, R. Moreno-Loshuertos, P. Fernandez-Silva, A. I. Gallego, L. Martinez-Lostao, A. Martinez, L. D. Carlos and A. Millan, *Nano Lett.*, 2020, **20**, 6466–6472.
11 Y. L. Shen, H. D. A. Santos, E. C. Ximendes, J. Lifante, A. Sanz-Portilla, L. Monge, N. Fernandez, I. C. Coria, C. Jacinto, C. D. S. Brites, L. D. Carlos, A. Benayas, M. C. Iglesias-de la Cruz and D. Jaque, *Adv. Funct. Mater.*, 2020, **30**, 2002730.
12 M. Xu, X. M. Zou, Q. Q. Su, W. Yuan, C. Cao, Q. H. Wang, X. J. Zhu, W. Feng and F. Y. Li, *Nat. Commun.*, 2016, **9**, 2698.
13 J. J. Zhou, B. del Rosal, D. Jaque, S. Uchiyama and D. Y. Jin, *Nat. Methods*, 2020, **17**, 967–980.

14 G. Brunet, R. Marin, M. J. Monk, U. Resch-Genger, D. A. Galico, F. A. Sigoli, E. A. Suturina, E. Hemmer and M. Murugesu, *Chem. Sci.*, 2019, **10**, 6799–6808.

15 D. Errulat, R. Marin, D. A. Galico, K. L. M. Harriman, A. Pialat, B. Gabidullin, F. Iikawa, O. D. D. Couto, J. O. Moilanen, E. Hemmer, F. A. Sigoli and M. Murugesu, *ACS Cent. Sci.*, 2019, **5**, 1187–1198.

16 R. A. S. Ferreira, E. Mamontova, A. M. P. Botas, M. Shestakov, J. Vanacken, V. Moshchalkov, Y. Guari, L. F. Chibotaru, D. Luneau, P. S. Andre, J. Larionova, J. Long and L. D. Carlos, *Adv. Opt. Mater.*, 2021, **9**, 2101495.

17 M. Fondo, J. Corredoira-Vazquez, A. M. Garcia-Deibe, J. Sanmartin-Matalobos, M. Amoza, A. M. P. Botas, R. A. S. Ferreira, L. D. Carlos and E. Colacio, *Inorg. Chem. Front.*, 2020, **7**, 3019–3029.

18 D. A. Galico, R. Marin, G. Brunet, D. Errulat, E. Hemmer, F. A. Sigoli, J. O. Moilanen and M. Murugesu, *Chemistry*, 2019, **25**, 14625–14637.

19 R. Jankowski, J. J. Zakrzewski, M. Zychowicz, J. H. Wang, Y. Oki, S. I. Ohkoshi, S. Chorazy and B. Sieklucka, *J. Mater. Chem. C*, 2021, **9**, 10705–10717.

20 K. Kumar, D. Abe, K. Komori-Orisaku, O. Stefanczyk, K. Nakabayashi, J. R. Shakirova, S. P. Tunik and S. Ohkoshi, *RSC Adv.*, 2019, **9**, 23444–23449.

21 S. Ma, T. Zhang, J. P. Zhao, Z. Y. Liu and F. C. Liu, *Dalton Trans.*, 2021, **50**, 1307–1312.

22 R. Marin, G. Brunet and M. Murugesu, *Angew. Chem., Int. Ed.*, 2021, **60**, 1728–1746.

23 A. Puzan, M. Zychowicz, J. H. Wang, J. J. Zakrzewski, M. Reczynski, S. Ohkoshi and S. Chorazy, *Dalton Trans.*, 2021, **50**, 16242–16253.

24 J. Wang, J. J. Zakrzewski, M. Heczko, M. Zychowicz, K. Nakagawa, K. Nakabayashi, B. Sieklucka, S. Chorazy and S. I. Ohkoshi, *J. Am. Chem. Soc.*, 2020, **142**, 3970–3979.

25 J. Wang, J. J. Zakrzewski, M. Zychowicz, V. Vieru, L. F. Chibotaru, K. Nakabayashi, S. Chorazy and S. I. Ohkoshi, *Chem. Sci.*, 2021, **12**, 730–741.

26 W. Wegner, J. J. Zakrzewski, M. Zychowicz and S. Chorazy, *Sci. Rep.*, 2021, **11**, 11354.

27 J. J. Zakrzewski, K. Kumar, M. Zychowicz, R. Jankowski, M. Wyczesany, B. Sieklucka, S. I. Ohkoshi and S. Chorazy, *J. Phys. Chem. Lett.*, 2021, **12**, 10558–10566.

28 R. G. Geitenbeek, A. E. Nieuwelink, T. S. Jacobs, B. B. V. Salzmann, J. Goetze, A. Meijerink and B. M. Weckhuysen, *ACS Catal.*, 2018, **8**, 2397–2401.

29 T. Hartman, R. G. Geitenbeek, G. T. Whiting and B. M. Weckhuysen, *Nat. Catal.*, 2019, **2**, 986–996.

30 J. Drabik and L. Marciniak, *ACS Appl. Mater. Interfaces*, 2021, **13**, 1261–1269.

31 O. A. Savchuk, J. J. Carvajal, C. Cascales, J. Massons, M. Aguilo and F. Diaz, *J. Mater. Chem. C*, 2016, **4**, 6602–6613.

32 (*a*) E. Coronado, *Nat. Rev. Mater.*, 2020, **5**, 86–104; (*b*) J. Ferrando-Soria, J. Vallejo, M. Castellano, J. Martinez-Lillo, E. Pardo, J. Cano, I. Castro, F. Lloret, R. Ruiz-Garcia and M. Julve, *Coord. Chem. Rev.*, 2017, **339**, 17–103.

33 F. Biscarini, E. Coronado, A. Painelli and M. Yamashita, *J. Mater. Chem. C*, 2021, **9**, 10521–10523.

34 K. Yamashita, R. Miyazaki, Y. Kataoka, T. Nakanishi, Y. Hasegawa, M. Nakano, T. Yamamura and T. Kajiwara, *Dalton Trans.*, 2013, **42**, 1987–1990.

35 F. Pointillart, B. Le Guennic, S. Golhen, O. Cador, O. Maury and L. Ouahab, *Chem. Commun.*, 2013, **49**, 615–617.

36 E. Mamontova, J. Long, R. A. S. Ferreira, A. M. P. Botas, D. Luneau, Y. Guari, L. D. Carlos and J. Larionova, *Magnetochemistry*, 2016, **2**, 41.

37 J. Long, R. Vallat, R. A. S. Ferreira, L. D. Carlos, F. A. A. Paz, Y. Guari and J. Larionova, *Chem. Commun.*, 2012, **48**, 9974–9976.

38 E. L. Gavey, M. Al Hareri, J. Regier, L. D. Carlos, R. A. S. Ferreira, F. S. Razavi, J. M. Rawson and M. Pilkington, *J. Mater. Chem. C*, 2015, **3**, 7738–7747.

39 J. J. Zakrzewski, M. Liberka, M. Zychowicz and S. Chorazy, *Inorg. Chem. Front.*, 2021, **8**, 452–483.

40 E. Huskowska, I. Turowska-Tyrk, J. Legendziewicz and J. P. Riehl, *New J. Chem.*, 2002, **26**, 1461–1467.

41 J. J. Zakrzewski, S. Chorazy, K. Nakabayashi, S. Ohkoshi and B. Sieklucka, *Chem. – Eur. J.*, 2019, **25**, 11820–11825.

42 S. V. Eliseeva, D. N. Pleshkov, K. A. Lyssenko, L. S. Lepnev, J. C. G. Bunzli and N. P. Kuzmina, *Inorg. Chem.*, 2011, **50**, 5137–5144.

43 V. Tangoulis, N. Panagiotou, A. Tasiopoulos, G. Itskos, M. Athanasiou, E. Moreno-Pineda, W. Wernsdorfer, M. Schulze and O. Malina, *Inorg. Chem.*, 2022, **61**, 2546–2557.

44 S. Gao, B. Q. Ma, Z. M. Wang, T. Yi, C. S. Liao, C. H. Yan and G. X. Xu, *Mol. Cryst. Liq. Cryst. Sci. Technol., Sect. A*, 1999, **335**, 913–922.

45 (*a*) B. Yan and Y. S. Song, *J. Coord. Chem.*, 2004, **57**, 49–54; (*b*) D. Visinescu, M. G. Alexandru, D. G. Dumitrescu, S. Shova, N. Moliner, F. Lloret and M. Julve, *CrystEngComm*, 2021, **23**, 4615–4626.

46 A. R. Alkaraghouli, R. O. Day and J. S. Wood, *Inorg. Chem.*, 1978, **17**, 3702–3706.

47 Oxford Diffraction, *CrysAlis CCD and CrysAlis RED*, Oxford Diffraction Ltd, Abingdon, Oxford, England, 2008.

48 G. M. Sheldrick, SHELXT - Integrated space-group and crystal-structure determination, *Acta Crystallogr., Sect. A: Found. Adv.*, 2015, **71**, 3–8.

49 L. J. Farrugia, WinGX suite for small-molecule single-crystal crystallography., *Appl. Crystallogr.*, 1999, **32**, 837–838.

50 Y. Xin, J. H. Wang, M. Zychowicz, J. J. Zakrzewski, K. Nakabayashi, B. Sieklucka, S. Chorazy and S. Ohkoshi, *J. Am. Chem. Soc.*, 2019, **141**, 18211–18220.

51 S. Chorazy, M. Rams, K. Nakabayashi, B. Sieklucka and S. I. Ohkoshi, *Chem. – Eur. J.*, 2016, **22**, 7371–7375.

52 S. G. Bodige, M. A. Zottola, S. E. McKay and S. C. Blackstock, *Mater. Res. Bull.*, 1998, 243–253.

53 E. Pilichos, E. Sanakis, E.-K. Maniaki, C. P. Raptopoulou, V. Psycharis, M. M. Turnbull and S. P. Perlepes, *Magnetochemistry*, 2019, **5**, 39.

54 K. Nakamoto, *Infrared and Raman Spectra of Inorganic and Coordination Compounds*, Wiley, New York, USA, 4th edn, 1986, pp. 107, 272–280.

55 M. Llunell, J. Casanova, J. Girera, P. Alemany and S. Alvarez, *Shape Measures and Associated Tools, v 2.1*, Univ. Barcelona, Barcelona, 2013.

56 J.-L. Liu, K. Yuan, J.-D. Leng, L. Ungur, W. Wernsdorfer, F.-S. Guo, L. F. Chibotaru and M.-L. Tong, *Inorg. Chem.*, 2012, **51**, 8538–8544.

57 F. Aquilante, J. Autschbach and R. K. Carlson, *J. Comput. Chem.*, 2016, **37**, 506–541.

58 B. O. Roos, R. Lindh and P.-Å. Malmqvist, *J. Phys. Chem. A*, 2004, **108**, 2851–2858.

59 B. O. Roos, R. Lindh and P.-Å. Malmqvist, *J. Phys. Chem. A*, 2005, **109**, 6575–6579.

60 A. Lunghi, F. Totti, R. Sessoli and S. Sanvito, *Nat. Commun.*, 2017, **8**, 14620.

61 C. D. S. Brites, A. Millán and L. D. Carlos, Lanthanides in Luminescent Thermometry, in *Handbook on the Physics and Chemistry of Rare Earths*, ed. J.-C. G. Bünzli and V. K. Pecharsky, Elsevier Science, B. V., Amsterdam, 2016, vol. 48, p. 339.

62 S. Balabhadra, M. L. Debasu, C. D. S. Brites, J. Rocha and L. D. Carlos, *J. Lumin.*, 2016, **180**, 25–30.

63 E. Moreno-Pineda and W. Wernsdorfer, *Nat. Rev. Phys.*, 2021, **3**, 645–659.

64 K. S. Kumar, D. Serrano, A. M. Nonat, B. Heinrich, L. Karmazin, L. J. Charbonniere, P. Goldner and M. Ruben, *Nat. Commun.*, 2021, **12**, 2152.

65 M. Suta and A. Meijerink, *Adv. Theor. Simul.*, 2020, **3**, 2000176.

66 A. N. C. Neto, E. Mamontova, A. M. P. Botas, C. D. S. Brites, R. A. S. Ferreira, J. Rouquette, Y. Guari, J. Larionova, J. Long and L. D. Carlos, *Adv. Opt. Mater.*, 2022, **10**, 2101870.